Ice and water droplets on graphite: A comparison of quantum and classical simulations

Cite as: J. Chem. Phys. **141**, 204701 (2014); https://doi.org/10.1063/1.4901562
Submitted: 14 August 2014 . Accepted: 27 October 2014 . Published Online: 24 November 2014

Rafael Ramírez, Jayant K. Singh, Florian Müller-Plathe, Michael C. Böhm, et al.

Ice and water droplets on graphite: A comparison of quantum and classical simulations

Rafael Ramírez,[1,a)] Jayant K. Singh,[2,3] Florian Müller-Plathe,[2] and Michael C. Böhm[2]
[1]*Instituto de Ciencia de Materiales de Madrid (ICMM), Consejo Superior de Investigaciones Científicas (CSIC), Campus de Cantoblanco, 28049 Madrid, Spain*
[2]*Eduard-Zintl-Institut für Anorganische und Physikalische Chemie and Center of Smart Interfaces, Technische Universität Darmstadt, Alarich-Weiss-Str. 4, 64287 Darmstadt, Germany*
[3]*Department of Chemical Engineering, Indian Institute of Technology Kanpur, Kanpur 208016, India*

(Received 14 August 2014; accepted 27 October 2014; published online 24 November 2014)

Ice and water droplets on graphite have been studied by quantum path integral and classical molecular dynamics simulations. The point-charge q-TIP4P/F potential was used to model the interaction between flexible water molecules, while the water-graphite interaction was described by a Lennard-Jones potential previously used to reproduce the macroscopic contact angle of water droplets on graphite. Several energetic and structural properties of water droplets with sizes between 10^2 and 10^3 molecules were analyzed in a temperature interval of 50–350 K. The vibrational density of states of crystalline and amorphous ice drops was correlated to the one of ice Ih to assess the influence of the droplet interface and molecular disorder on the vibrational properties. The average distance of covalent OH bonds is found 0.01 Å larger in the quantum limit than in the classical one. The OO distances are elongated by 0.03 Å in the quantum simulations at 50 K. Bond distance fluctuations are large as a consequence of the zero-point vibrations. The analysis of the H-bond network shows that the liquid droplet is more structured in the classical limit than in the quantum case. The average kinetic and potential energy of the ice and water droplets on graphite has been compared with the values of ice Ih and liquid water as a function of temperature. The droplet kinetic energy shows a temperature dependence similar to the one of liquid water, without apparent discontinuity at temperatures where the droplet is solid. However, the droplet potential energy becomes significantly larger than the one of ice or water at the same temperature. In the quantum limit, the ice droplet is more expanded than in a classical description. Liquid droplets display identical density profiles and liquid-vapor interfaces in the quantum and classical limits. The value of the contact angle is not influenced by quantum effects. Contact angles of droplets decrease as the size of the water droplet increases which implies a positive sign of the line tension of the droplet. [http://dx.doi.org/10.1063/1.4901562]

I. INTRODUCTION

The structure and dynamics of water at interfaces play an important role in various industrial, geological, and biological processes.[1–3] The nature of the substrate changes the behavior of water and ice on the interface. While strong binding of water on hydrophilic substrates is expected, even hydrophobic ones can affect appreciably the water structure near the surface.[4,5] In recent years, a hydrophobic substrate such as graphite has gained significant attention, due to its improved thermal, mechanical, and electronic properties.[6–8] In particular, the interaction of water and ice with graphene has been investigated immensely because of its importance as a material for coating in electrodes and membranes for water treatment,[9,10] and as a lubricant.[11,12]

The understanding of ice-surface interactions is vital in the design of anti-ice surfaces. In the past years, such investigations have been motivated by superhydrophobic surfaces.[13] Recently, the structural stability of different ice bilayers on graphene has been discussed in a density functional theory (DFT) study of Anick on the ice-graphene interaction.[14] Similarly, Ambrosetti *et al.* studied the water and ice interaction with graphite using *ab initio* DFT calculations in order to address the lubricating effects of water on graphite and graphene surfaces.[15] Singh and Müller-Plathe investigated the freezing temperature and adhesion of ice droplets on graphite-based smooth and rough surfaces using a coarse-grained model.[16] However, neither the aforementioned works nor numerous other simulations dealing with interfacial properties of water and ice on graphitic surfaces addressed the limitations of using the classical limit to describe the atomic nuclei.[17–24] The classical approach does not consider the spatial fluctuations that appear on the basis of quantum mechanical zero-point movements. Therefore, the thermodynamic properties derived in the quantum and classical limits may differ. We will employ the notation "nuclear quantum effect" to characterize the difference in the properties of water molecules when one compares the quantum and classical descriptions of the atomic nuclei.

A recent investigation of the water-vapor interface by interface-specific vibrational spectroscopy included a quantum treatment of the atomic nuclei by path integral (PI)

a)Electronic mail: ramirez@icmm.csic.es

simulations.[25] Specifically, the bond orientation of water at the water-vapor interface depends on the water isotope (H-D) composition. Interestingly, the interfacial water structures of H_2O and D_2O were indistinguishable while the intramolecular symmetry breaking in HDO has implications on the bond orientation at the surface. Isotope effects in the properties of HDO are caused by quantum effects associated with the different H/D nuclear masses. The classical limit predicts that all structural equilibrium properties are invariant with respect to the nuclear mass.

In recent combined PI-*ab initio* or density functional simulations of spectroscopic properties of hydrocarbon compounds, we have shown that nuclear quantum effects are of sizeable importance even in the vicinity of room temperature. We have analyzed UV-vis and photoelectron spectra, as well as hyperfine splitting constants and NMR chemical shifts.[26–28] The experimental inverse isotope effect in the lattice parameter of ice Ih has been explained recently by a combination of DFT calculations of phonon properties and PI simulations.[29] The isotope effect in the melting point of ice Ih and the negative thermal expansion of ice Ih at low temperatures has been reproduced realistically by quantum PI simulations.[30,31] On the basis of this experience our main interest in the present paper is the comparison of classical and quantum PI simulations of ice and water droplets on graphite in order to assess the possible significance of nuclear quantum effects in structural, energetic, and wetting properties of the system. However, isotope effects resulting from the substitution of H by D are not treated in this study.

Our present simulations will employ a flexible point-charge model (q-TIP4P/F) of water which was parametrized to be used in quantum PI simulations.[32] The water-carbon interaction is treated by the Lennard-Jones (LJ) parametrization of Werder *et al.*[17] These authors showed a linear relation between the contact angle of water and the surface binding energy of a single water molecule. As a matter of fact, the employed parametrization recovers the macroscopic contact angle of water on graphite of 86°.[17] This model has been adopted previously to study the work of adhesion of water as a function of the number of layers in the graphitic substrate. It shows the independence of the contact angle of water droplets from the number of layers in bi- and multilayered graphene.[24] Our selection of an empirical water-graphite model with known wetting properties is justified as we do not aim at solving any of the controversial results concerning the wetting properties of water on graphitic systems.[20,23,33,34] Rather, we adopt a simple model of known wetting properties to address the question if contact angles derived in the classical limit will be different than those derived by a quantum treatment of the atomic nuclei.

The layout of the paper is the following. Computational details of the simulations of water on graphite are given in Sec. II. Quantum effects in the binding energy of a water dimer and the surface binding energy of a water molecule are presented in Sec. III as a function of temperature. The structural analysis of the hydrogen bond (H-bond) network of ice and water droplets is presented in Sec. IV. The generation of ice droplet configurations as well as some structural and vibrational properties of optimized configurations are discussed in Sec. IV A. In the discussion, we have to discriminate the strong intramolecular OH bonds from the weaker hydrogen bonds. We will demonstrate that nuclear quantum effects are of different importance in the two types of bonds. Particular emphasis is given to the differences between the quantum and classical expectations of bond distances and their respective fluctuations as a function of temperature (Secs. IV B and IV C). The temperature dependence of the kinetic and potential energy of ice and liquid droplets as well as their atomic density profiles are analyzed in Sec. V by classical and quantum simulations. The results of the quantum and classical interfacial properties of water droplets at 300 K are presented in Sec. VI. The paper closes with the conclusions.

II. COMPUTATIONAL CONDITIONS

The PI formulation allows the computation of thermodynamic equilibrium properties in the quantum limit by using an isomorphism with a specific classical system. This isomorphism implies that the quantum partition function can be derived with arbitrary numerical accuracy in terms of that of the classical isomorph. However, the isomorphism does not apply to the dynamic (time dependent) properties of the quantum system. Specifically, the classical isomorph is constructed by representing each quantum particle (here, atomic H and O nuclei of the water molecules) by a set of L particles linked together in the form of a ring polymer. These particles are often called replicas or beads. The PI formulation leads to an expression for the potential energy of this set of particles that is employed in PI simulations to approach the quantum limit of thermodynamic properties. Each bead in the ring interacts with its two neighbors by a harmonic spring with a temperature- and mass-dependent force constant. Details of this powerful simulation method can be found in Refs. 35–39. Within the PI approach, equilibrium properties may be derived by a classical molecular dynamics (MD) algorithm applied to the classical isomorph. Technical details for performing efficient PIMD simulations using effective reversible integrator algorithms have been described in Refs. 40–43.

The present PIMD and classical MD simulations of ice and water droplets on graphite are performed at temperatures between 50 and 350 K. Graphite is simulated as two staggered graphene sheets with an interlayer distance of 3.35 Å along the perpendicular z-direction. The covalent CC bond length amounts to 1.42 Å. Carbon atoms are maintained fixed at their initial positions. This approximation has little effect on the contact angle of the water droplets but reduces the computational cost significantly.[17] For the simulations of droplets with less than 700 water molecules, the graphene sheet is defined by a rectangular supercell (compatible to the hexagonal symmetry of graphene) with $x \times y$ dimensions of 63.9 $\times$ 73.8 Å^2, including 1800 C atoms per sheet. A larger sheet with dimensions 85.2 $\times$ 98.4 Å^2, containing 3200 C atoms per sheet, was used for the simulations of larger water droplets. Periodic boundary conditions were applied in the x, y-plane. A reflecting wall was set roughly 7 Å above the top of the water droplet.

The interaction between water molecules and the C atoms was calculated by the Werder *et al.* parametrization[17] of a LJ potential between O and C atoms. In the model, there is no LJ interaction between the C and H centers. The employed parameters are $\epsilon_{CO} = 0.392$ kJ/mol and $\sigma_{CO} = 3.19$ Å with a cut-off distance of 10 Å. For water we use the flexible point-charge model q-TIP4P/F, that was originally parametrized to provide the correct liquid structure, diffusion coefficient, and infrared adsorption spectrum in quantum PI simulations.[32] The cut-off for the LJ interaction between O atoms in the q-TIP4P/F model was 10 Å. The LJ interactions (both CO and OO) were shifted by a constant corresponding to the potential value at the cut-off distance. The Coulomb potential between the water molecules in the droplet was calculated by a minimum image convention in the x, y-plane so that the Coulomb interaction between periodically repeated drops was excluded from the calculation.

The number of beads in the PIMD simulations was set as the integer number closest to fulfill the condition $LT = 6000$ K, i.e., at 300 K the number of beads was $L = 20$, while at 50 K it was $L = 120$. This condition has been applied in previous water and ice simulations with the same model potential.[30,31,44–46] A staging transformation was employed for the bead coordinates. This linear transformation was introduced to diagonalize the harmonic coupling between neighboring beads.[43] The temperature was controlled by chains of four Nosé-Hoover thermostats coupled to each of the staging variables.[41] For the evolution of thermostats and harmonic bead interactions, a time step of $\delta t = \triangle t/4$ was used, where $\triangle t$ is the time step adopted for the calculation of the q-TIP4P/F and LJ forces. A value $\triangle t = 0.2$ fs provides adequate convergence. The virial estimator was employed for the calculation of the kinetic energy.[47,48] The classical limit is achieved by setting $L = 1$ in the PIMD algorithm. This setup implies that the staging coordinates become identical to the positions of the nuclei and that the harmonic bead interaction vanishes in the classical limit.

Typical simulations for liquid droplets consist of an equilibration run of 2 ns followed by a production run of 3 ns for the calculation of equilibrium properties. For the analysis of the liquid-vapor interface, longer runs of 12 ns were performed to check the convergence of the results. Statistical uncertainties were evaluated by dividing the total simulation run into three blocks and by calculating the standard deviation of the block averages. At low temperatures, i.e., in the case of ice droplets, shorter simulation runs of 0.2 ns were sufficient to obtain a statistical precision similar to that of a liquid droplet.

III. WATER DIMER AND WATER-GRAPHITE INTERACTIONS

Before presenting our ice and water droplet simulations, the employed model potential is tested by the study of the quantum effect in the binding energy of a water dimer as well as in the surface binding energy of a water molecule and water dimer. Particular emphasis is laid on the difference between quantum and classical results and on the comparison with available experimental and theoretical data.

A. Water dimer binding energy

The binding energy of a water dimer $(H_2O)_2$ is calculated as

$$E_d = E[(H_2O)_2] - 2E[H_2O] \,, \tag{1}$$

where E is the total internal energy of the given molecule. E is made up of a sum of kinetic (K) and potential (U) energy contributions so that

$$E_d = U_d + K_d \,. \tag{2}$$

The quantum limit for E_d and U_d is displayed in Fig. 1 as a function of temperature by continuous and broken lines, respectively. The classical results are shown by a dotted line. The classical binding energy of the water dimer at $T = 0$ K is $D_e = -27.4$ kJ/mol. The extrapolated quantum value at $T = 0$ amounts to $D_0 = -18.6$ kJ/mol. As a consequence of the zero-point motion, the absolute value of the dimer binding energy in the quantum limit is 8.8 kJ/mol (about 32%) smaller than the classical value. The zero-point effect can be separated into potential (4.7 kJ/mol) and kinetic energy (4.1 kJ/ mol) contributions. Note that both terms should be identical for a purely harmonic interaction so that their difference is caused by the anharmonicity of the intermolecular H-bond in the employed potential model. The difference between the quantum and classical binding energies decreases with temperature so that at 150 K it is reduced to 3.6 kJ/mol.

As a consequence of the equipartition principle, the kinetic energy of the dimer is identical in the classical limit to that of two separated water molecules. The reason is the equality in the total number of degrees of freedom (vibrational, rotational, and translational, summing up to 18 is both cases). Thus, the classical binding energy E_d becomes identical to the potential energy difference, U_d, at all temperatures. The calculated equilibrium OO distance in the dimer amounts to 2.84 Å in the quantum limit at 20 K while it is shorter by 0.06 Å (2.78 Å) in the classical case.

Our estimate of the zero-point effect in the binding energy of the dimer at $T = 0$ is in reasonable agreement with

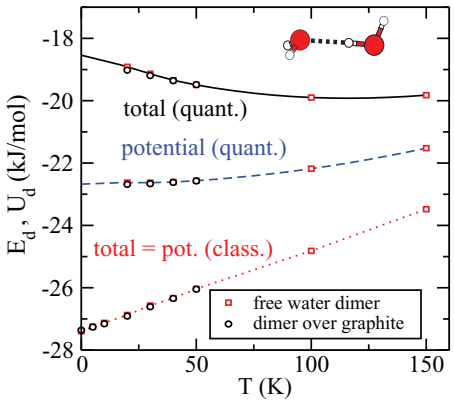

FIG. 1. Binding energy, E_d, of the water dimer as a function of temperature which has been derived from simulations with the q-TIP4P/F model. The continuous and broken lines are the total (E_d) and potential (U_d) energies in the quantum limit, while the dotted line shows the classical result. Open squares were obtained in vacuum (up to 150 K), circles on a graphite surface (up to 50 K). Both sets of results are nearly identical. The molecular structure of the dimer is displayed. The lines are guides to the eyes.

the result (7.2 kJ/mol) derived from an average of several intermolecular potential energy models and a harmonic treatment of the intramolecular vibrations.[49] The value derived by Shank *et al.* from an accurate *ab initio* potential energy surface is 7.6 kJ/mol.[50] This study predicts a binding energy of $D_0 = -13.2$ kJ/mol in the quantum limit, a result in quantitative agreement with an *a posteriori* experimental study using velocity-map imaging and resonance-enhanced multiphonon ionization.[51] Note that the empirical q-TIP4P/F model overestimates the binding energy D_0 of the dimer by 5.5 kJ/mol (about 40%) at $T = 0$. We recall that this empirical potential was optimized for condensed matter simulations.[32] In Sec. V, it is shown that the sublimation enthalpy of ice Ih is reproduced with an improved accuracy.

The open squares in Fig. 1 represent the binding energy of a water dimer in vacuum, while open circles were derived for a dimer bonded on a graphite surface. Note that both results are nearly identical, i.e., the graphite surface does not affect the dissociation energy of the dimer. Such a result indicates that with the employed potential both the water dimer and water-graphite interactions can be optimized simultaneously without showing competing effects.

B. Surface binding energy

The surface binding energy of a cluster $(H_2O)_n$ of n water molecules on graphite is calculated as

$$E_s = \frac{1}{n}[E[(H_2O)_n/\text{Graphite}] - E[(H_2O)_n]] \, . \qquad (3)$$

Note that the factor $1/n$ normalizes the value of E_s; the graphite energy does not appear in the adopted formula as it is treated as a rigid wall. The results for a molecule ($n = 1$) and a dimer ($n = 2$) are shown in Fig. 2 up to 50 K. At higher temperatures, an isolated water molecule escapes from the graphite surface during the simulation run. The classical E_s at $T = 0$ amounts to about -6 kJ/mol for both values of n. We have checked that our result is consistent with the binding energy (-6.33 kJ/mol) derived previously for one molecule with the same water-graphite potential model.[17] The small numerical difference is caused by the shift in the LJ potential between O and C that we apply at the cut-off distance. An extrapolation of the quantum binding energy at $T = 0$ gives an absolute value that is roughly 0.4 kJ/mol smaller (7%) than in the classical limit. At $T = 50$ K, this difference has been reduced to less than 0.1 kJ/mol. The surface binding energy of water with the employed model potential is about 3 times smaller than the binding energy of the H-bond in the water dimer.

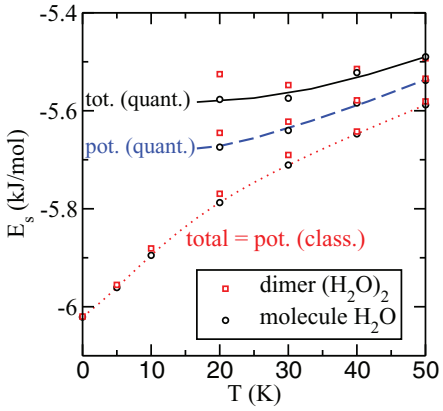

FIG. 2. Surface binding energy, E_s, of a water molecule (open circles) on graphite up to 50 K. The continuous and broken lines indicate the total and potential energies in the quantum limit, while the dotted line shows the classical result. The lines are guides to the eye. The corresponding results for a water dimer are shown as open squares.

The normalized surface binding energy E_s of a water dimer is similar to the one of an isolated molecule. Recall that the employed empirical potential, fitted to reproduce the macroscopic contact angle of water droplets, is only a function of the relative position of the oxygen atoms with respect to the graphite surface. It is independent of the orientation of the water molecule that is determined by the position of the H atoms. A DFT study using a generalized gradient approximation (GGA) shows that the normalized surface binding of a water dimer depends on its orientation. The reported surface binding energy is rather low and its absolute value varies in the range 1.4–2.7 kJ/mol for three different orientations. For water clusters with 3 and 5 molecules, however, the reported DFT binding energy does not depend on the cluster orientation.[52]

The surface binding energy of a water monomer on graphitic surfaces has been the subject of a large number of studies. Experiments, however, are somewhat obstructed because the water molecules tend to form clusters. Theoretical methods, too, are difficult in their realization because the graphite-water interaction is due to dispersion forces.[53] Feller and Jordan estimated an absolute value of the surface binding energy of 24.3 ± 1.5 kJ/mol by extrapolating the results of Møller-Plesset perturbation theory in clusters up to 37 fused benzene rings.[54] This value is similar to the H-bond binding energy of a water dimer. In the optimized geometry, the water molecule is oriented with one H atom pointing toward a carbon atom of a ring.[54] Bermudez and Robinson reported a binding energy of 20 kJ/mol using DFT and including dispersion forces.[55] A density-functional/coupled-cluster (DFT/CC) study predicts a significantly lower interaction energy of 15 kJ/mol, with a "down" structure where both hydrogen atoms of water are pointing toward the graphite plane.[56] The same structure is predicted by a coupled-cluster approach with single, double, and connected triple excitations (CCSD(T)) leading to a binding energy of 13 kJ/mol.[57] Moreover, the surface binding energy depends strongly on the orientation of the water molecule. It is reduced to 10.6 kJ/mol if the H atoms are oriented pointing outwards the graphite surface.[57] A calculation of an extended model of graphene using diffusion Monte Carlo (DMC), random phase approximations (RPA), and various DFT functionals comes to the conclusion that the absolute value of the water binding energy should be in the range 9.4–6.7 kJ/mol.[53] The previously commented DFT-GGA study by Leenaerts *et al.* reports an even smaller value of 2.8 kJ/mol for the binding energy of a water monomer on a graphene sheet.[52]

The sizeable dispersion of *ab initio* data for the binding energy of a single water molecule justifies our selection of an empirical parameterization. The numerical difficulties of an

ab initio treatment of droplets with 10^2–10^3 water molecules are orders of magnitude larger than those of a single molecule. In our study, we prioritize the investigation of quantum effects in properties such as the contact angle of liquid droplets. The employed empirical potential is independent of the water orientation and the graphite surface is treated as a static rigid wall. These approximations have been shown to be reasonable in the classical limit to describe the weak physisorption of water droplets on graphite.[17,24] Recent quantum simulations of the liquid-vapor interface of water have also employed empirical models.[25] Thus, it can be assumed that the parameterization of Werder *et al.*[17] aims at describing the surface interaction of an average water orientation as encountered at the interface of a large water droplet. Thus, we have to expect that the model underestimates the binding energy for an optimized orientation of a water monomer.

IV. STRUCTURAL ANALYSIS OF THE DROPLETS

A. Initial configurations

At temperatures where the droplet is solid, the simulations are expected to depend strongly on the initial configuration. This follows from the fact that molecular diffusion in a solid cluster is hindered by high energy barriers. As liquid droplets with the employed potential model are expected to have contact angles around 90°,[17] initial ice droplet configurations were generated with the form of a half sphere. To this aim, a Monte Carlo procedure was used to generate a proton disordered structure of ice Ih with nearly zero dipole moment.[58] The hexagonal ice Ih is the stable phase of ice at atmospheric pressure.

We define the hexagonal axis of ice Ih parallel to the z-direction, see Fig. 3. Then a cluster is selected by adding successive coordination spheres around an arbitrary water molecule of the ice crystal. The first coordination sphere consists of four H-bonded molecules with tetrahedral ordering.

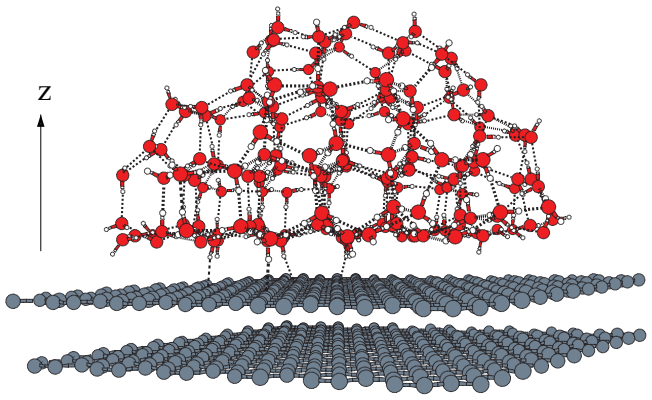

FIG. 3. Geometry of the optimized crystalline ice droplet D_{187} over graphite. The z-direction is perpendicular to the graphite surface. The topmost graphite layer is set at $z = 0$. The water molecules in the starting configuration belong to a cluster with Ih ice structure. Layers of water molecules parallel to the graphite surface correspond to crystallographic 0001 planes. Four of such layers are visible. These basal planes in ice Ih are made up of puckered hexagonal rings of O atoms in a chair conformation (i.e., they are not planar). The disruption of the tetrahedral H-bond network at the droplet surface generates disorder such as OH dangling bonds and water molecules having 2 or three H-bonds.

One of these H-bonds is oriented parallel to the hexagonal z-axis. A perpendicular plane cutting this H-bond will divide the spherical cluster into two parts. The spherical cap containing the central molecule is then used as initial configuration for the simulations. By considering different numbers of coordination spheres we have generated crystalline ice droplets, D_n, with varying number of water molecules, $n = 187$, 377, 678, and 1071.

In addition, an initial amorphous ice structure was generated for the droplet D_{377} by sudden cooling of the final configuration of a liquid drop simulated at 300 K. The reported freezing temperature of the employed water model at ambient pressure amounts to 251 K.[32] The influence of the droplet free energy is expected to lower the freezing point.[59] A recent simulation has estimated a reduction of about 6 K in the freezing temperature of water nanodroplets relative to the liquid bulk.[16]

In the initial step of the simulations, we want to characterize some structural properties related to the molecular disorder in the ice droplet. To this aim a geometry optimization of the D_n droplets was performed. We have performed a simulated annealing cycle by classical MD at temperatures between 200 and 20 K with a cooling rate of 6 K ps^{-1} in all calculations.[60] The highest temperature allows thermally activated jumps across energy barriers. Nevertheless, it is low enough to avoid the melting of the ice cluster. At the end of the annealing cycle, a conjugate gradient algorithm was applied to obtain an optimized structure. The geometrical arrangement of such a crystalline D_{187} droplet on graphite is shown in Fig. 3. The optimized structures of all D_n droplets are collected in the supplementary material.[61]

The structural analysis requires the identification of H-bonds in the droplet structure. To this aim we have employed the geometrical definition of Ref. 62. If O1−H is a covalent bond of a water molecule, then the three-center unit O1−H···O2 contains a H-bond if the three following conditions are satisfied: (i) the distance between O1 and O2 is lower than 3.2 Å; (ii) the H···O2 distance is shorter than 2.4 Å; (iii) the angle between the O1−H and O1O2 directions is lower than 30°. Here, the atom O1 is the donor (D) and O2 the acceptor (A) in the H-bond. In the droplet, the "type" of an oxygen atom is defined by the number of H-bonds in which it is a donor and the number in which it is an acceptor.[63] For example, DAA refers to an O atom (or H_2O molecule) having three H-bonds. It acts as an acceptor in two H-bonds, and as a donor in one. Therefore, it has additionally one covalently bonded H forming an OH dangling bond. In the ideal Ih ice structure, all oxygen atoms are DDAA without OH dangling bonds present in the crystal.

The different types of O atoms in a droplet can be discriminated unambiguously by considering their number of dangling and acceptor H-bonds. In Table I, we summarize this criterion. In addition, the relative concentration of the different types of O atoms in the optimized structure of the D_{377} droplet is given for the crystalline and amorphous case. The disorder in the H-bond network of the ice droplets is recognized by the presence of O atoms different from DDAA. The optimized crystalline droplet D_{377} shows a significant presence of DDA and DAA units. The main difference with the

TABLE I. The first three columns discriminate the different types of O atoms in a droplet by the number of OH dangling (n_d) and acceptor H-bonds (n_{acc}) in the given H_2O molecule. n_{tot} is the total number of H-bonds to which the molecule participates. The relative concentration of the different O atoms found in the optimized crystalline (c) and amorphous (a) droplet D_{377} is compared to an ideal ice Ih structure. The presence of O atoms different from DDAA is a consequence of the disorder in the H-bond framework.

O type	n_d	n_{acc}	n_{tot}	D_{377} (c)	D_{377} (a)	Ice Ih
A	2	1	1	0	0	0
D	1	0	1	0	0	0
DA	1	1	2	2%	3%	0
DAA	1	2	3	13%	9%	0
DDA	0	1	3	16%	15%	0
DDAA	0	2	4	67%	68%	100%
DDAAA	0	3	5	2%	6%	0

optimized amorphous droplet is the larger number of DDAAA atoms (i.e., 5 coordinated water molecules) in the amorphous case.

The molecular disorder affects the collective vibrations of the ice droplets. In Fig. 4, the harmonic vibrational density of states (VDOS) for the optimized crystalline structure of the ice droplet D_{377} is compared with that of ice Ih. The vibrational states can be divided into four separated regions. They are shown in three sub-plots. The stretching band of the ice drops is split into two bands (see Fig. 4(c)). The peak above 3790 cm^{-1} originates from the presence of dangling OH bonds in the droplet. The blue shift of the OH stretching at water interfaces has been demonstrated by sum-frequency vibrational spectroscopy which specifically can probe molecules at interfaces,[64] by high-resolution electron energy loss spectroscopy (HREELS),[65] as well as by MD simulations with flexible water models.[18] The VDOS curve of ice Ih has a gap in the region $400 < \omega < 520$ cm^{-1}. In this region, the VDOS of the crystalline ice drops displays the presence of librational states (see Fig. 4(a)). These low frequency librations are related to the hindered rotations of water molecules at the interface. The comparison of the VDOS curves of the amorphous and crystalline ice droplets indicates that the librational band in the amorphous case is shifted to lower wavenumbers. This implies weaker H-bonds in the amorphous structure.

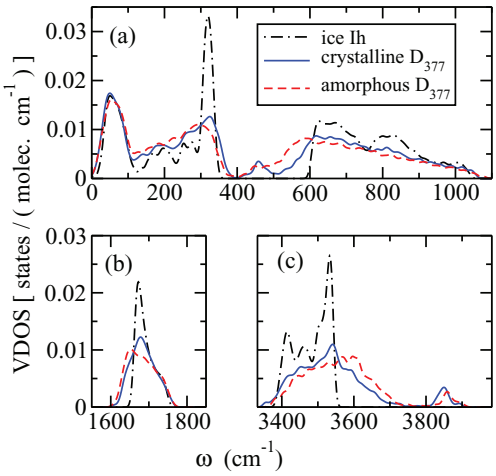

FIG. 4. Harmonic vibrational density of states of the optimized crystalline and amorphous ice droplet, D_{377}, over graphite as well as results of ice Ih. The vibrational states appear in three separate regions: (a) intermolecular translational and librational bands related to the H-bond framework; (b) intramolecular bending bands; (c) intramolecular stretching bands. A Gaussian broadening with full width at half maximum (FWHM) equal to 10 cm^{-1} was used to plot the vibrational states.

A recalculation of the VDOS without the water-graphite interaction shows that the graphite surface affects only the translational modes of water at wavenumbers below 150 cm^{-1}. The effect of the surface is visible by a shift of about 70 cm^{-1} to higher wavenumbers of those translational modes associated to the oxygen atoms lying directly above the graphite surface. We recall that the graphite surface was modeled as a rigid wall. Thus, the surface phonon coupling between flexible graphite and the water droplet is not included in our model.

The optimized ice droplets have been used as initial configuration for quantum and classical simulations at temperatures in the range 50–350 K. We have checked that at those temperatures where the droplet is liquid, the equilibrium simulations are indeed independent of the initial configuration. This check was made by additional droplet simulations with the O atoms located at the vertices of a simple cubic lattice with a cell parameter of 3 Å.

B. Temperature-dependent changes in the H-bond framework

The concentration of the different O atoms obtained by the quantum PIMD simulations of the D_{377} droplet is presented in Table II as a function of temperature. At 50 K the amorphous ice droplet differs from the crystalline one by having a significantly larger number of highly coordinated DDAAA molecules. In addition, it has a lower number of DAA centers. The ice droplet shows a relatively smooth change in the O species as a function of temperature up to 200 K. The main temperature effect is a reduction in the proportion of DAA molecules together with an increase in the number of DA centers. This fact is related to the increased molecular disorder of the ice droplet surface as a function of temperature. At 300 K the droplet is liquid. The melting of the droplet causes a large decrease in the number of DDAA molecules. The significant amount of D and A molecules in the liquid drop is a fingerprint for the presence of a liquid-vapor interface.

TABLE II. Concentration of the different types of O atoms found in quantum PIMD simulations of the droplet D_{377} as a function of temperature. At 50 K the results are shown for the amorphous (a) and the crystalline (c) ice droplet. The presence of A and D centers at 300 K and 350 K and is a fingerprint for the liquid-vapor interface.

O type	50 K (a)	50 K (c)	100 K	200 K	300	350 K
A	0	0	0	0	3%	6%
D	0	0	0	0	2%	4%
DA	3%	2%	3%	6%	15%	20%
DAA	8%	15%	14%	9%	11%	12%
DDA	14%	16%	16%	14%	25%	27%
DDAA	70%	66%	68%	68%	40%	29%
DDAAA	5%	1%	1	2%	3%	2%

TABLE III. Structural results from the quantum PIMD simulations of the droplet D_{377} as a function of temperature. At 50 K the data are shown for the amorphous (a) and the crystalline (c) ice droplets. The first row displays the concentration of OH dangling bonds with respect to the total number of OH bonds (i.e., 754 bonds). The next three rows indicate the relative distribution of the dangling bonds between the external droplet surface, toward graphite, and inside the drop. The next row shows the average number of H-bonds per water molecule ($\overline{n}_{HB}$). The last three lines are average OO distances for H-bonds between different types of molecules. The descriptor "short OO" indicates the average result for DDAA−DDA, DAA−DDAA, and DAA−DDA bonds. The symbol "long OO" refers to the average OO distance for DDA−DDAA, DDAA−DAA, and DDA−DAA bonds. The first molecule of a given H-bond denotes the donor unit, while the second is the acceptor unit.

	50 K (a)	50 K (c)	100 K	200 K	300 K	350 K
Dangling OH	6%	8%	8%	8%	16%	22%
(Droplet surface)	70%	64%	63%	65%	46%	45%
(Toward graphite)	21%	36%	36%	21%	14%	10%
(Inside the drop)	9%	0%	1%	14%	40%	45%
$\overline{n}_{HB}$	1.879	1.827	1.828	1.807	1.548	1.400
DDAA−DDAA	2.793	2.765	2.771	2.797	2.828	2.837
Short OO	2.774	2.765	2.769	2.792	2.805	2.837
Long OO	2.840	2.832	2.835	2.851	2.850	2.855

The structural analysis of the different O atoms obtained from classical simulations of the D_{377} droplet provides similar results as shown in Table II. The main difference is that the concentration of DDAA molecules for the liquid drop is about 2% larger in the classical limit. Comparison of quantum and classical simulations of bulk water shows that the classical limit implies a more structured liquid with an enhanced strength of the H-bonds.[66] The higher number of DDAA sites found in the classical droplet simulations is in line with this observation.

The temperature dependence of the relative number of OH dangling bonds in the droplets is summarized in Table III. This number is somewhat lower in the amorphous ice droplet (6%) than in the crystalline one (8%). This fact is related to the lower number of DAA molecules in the amorphous structure (see Table II). It is interesting to analyze the distribution of OH dangling bonds in three spatial regions: near the droplet surface, toward graphite, and inside the droplet. The criteria to differentiate the droplet surface and the inside domain considers the fact that the shape of the droplet is a spherical cap (see Sec. VI B). For a spherical cap of radius R_d, the boundary between the surface region and the droplet inside was located at $R_s = R_d - 1.5$ Å. In the ice droplet, most OH dangling bonds are located at the droplet surface. At 50 K, the amorphous structure shows dangling bonds inside the drop which are absent in the crystalline one. However, at 200 K the crystalline drop displays a distribution of dangling bonds that is similar to the amorphous one at 50 K. The total number of dangling bonds increases sharply in the liquid drop showing a similar proportion of dangling bonds at the surface and inside the drop.

The temperature dependence of the average number of H-bonds per molecule, $\overline{n}_{HB}$, is summarized in Table III. A tetrahedral H-bond framework, as found in ice Ih, is characterized by $\overline{n}_{HB} = 2$. This value is consistent with the fact that in a tetrahedral H-bond framework each molecule participates in 4 H-bonds. Note the strong reduction of $\overline{n}_{HB}$ upon the melting of the ice droplet. The presence of different O atoms also implies the possibility of different H-bond strengths and lengths. A H-bond can be specified by giving the type of the donor followed by the type of the acceptor, e.g., all H-bonds in ice Ih are DDAA−DDAA. *Ab initio* calculations show a significant difference in the H-bond length depending on whether it is DAA−DDAA or DDAA−DDA (shorter) vs DDA−DDAA or DDAA−DAA (longer).[63] Shorter H-bonds are associated to a combination where either the donor molecule is a single donor (i.e., D instead of DD) or the acceptor molecule is a single acceptor (i.e., A instead of AA). We have checked that the employed q-TIP4P/F force field is able to reproduce this subtle difference. In the last three rows of Table III, we compare the average OO distance of the DDAA−DDAA H-bonds with the distances derived for other types of H-bonds labeled as "short OO" and "long OO" units. The group labeled as "short OO" has OO distances similar to the DDAA-DDAA bond. The only exception is the amorphous droplet at 50 K. Here, the DDAA−DDAA bond is 0.03 Å longer than in the crystalline structure at the same temperature, i.e., this H-bond is weaker in the amorphous droplet. The OO distance in the "long OO" set of H-bonds are 0.07 Å larger than those in the "short OO" set at 50 K. This length difference is significant. A recent experimental study of average OO distances in water and ice by the study of the nearest-neighbor oxygen-oxygen radial distribution obtained by X-ray Raman based extended EXAFS spectroscopy report a value of 2.76 Å for ice and 2.81 Å for water, i.e., a difference of 0.05 Å.[67]

C. Quantum vs classical bond distances

A comparison of the quantum and classical results for the covalent OH distances in the D_{377} droplet is displayed in Fig. 5. In addition to the average distance, we also display the root mean square (RMS) fluctuations of the bond

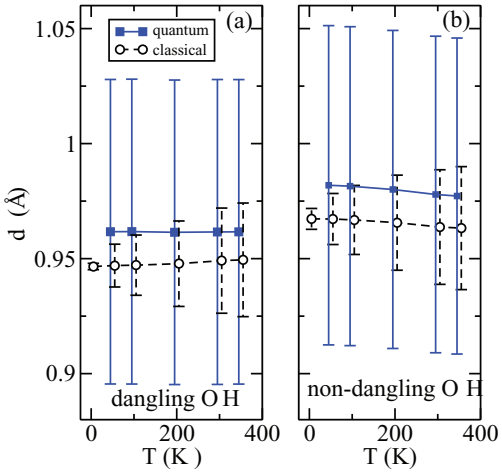

FIG. 5. Average OH distances d found in quantum and classical simulations of the droplet D_{377} as a function of temperature. The total length of the bars is two times the root mean square fluctuations around the distance d. Results are given for (a) dangling and (b) non-dangling OH bonds. For the sake of clarity, the quantum (classical) results were mutually displayed by ±5 K.

distance. In the quantum limit, the RMS fluctuations of the OH distance amount to 0.07 Å. These spatial fluctuations are a consequence of the atomic zero-point vibration. It is temperature independent up to the highest studied temperature (350 K). An OH dangling bond is shorter than a non-dangling one. In the non-dangling case, the H atom is also part of a H-bond. Both types of bonds display competing effects in their bonding strength.[29] It is interesting to note that the length of the non-dangling OH bonds (Fig. 5(b)) decreases slightly with increasing temperature while the length of the dangling bonds is temperature independent. This result reflects the anticorrelation between the covalent and the H-bond involving the same H atom. Any external factor such as temperature that causes an increase in the H-bond length implies the opposite effect on the non-dangling covalent OH bond.

The average OH distance in the classical limit is lower than in the quantum one. The classical bond fluctuations are much smaller than in the quantum case. The classical bond fluctuations at $T = 0$ are a consequence of the static molecular disorder. With increasing temperature these bond fluctuations increase, but even at 350 K they remain lower than the quantum ones.

The average distance and the RMS fluctuations of the DDAA−DDAA H-bonds are displayed in Fig. 6. The difference between the quantum and classical H···O distance at 50 K amounts to 0.05 Å. The increase of the bond distances with temperature is an effect due to the anharmonicity of the interatomic potential. The largest H-bond fluctuations are observed for the quantum simulations, although classical and quantum fluctuations become similar at 300 K. Note the relatively large fluctuations of the H-bond distance in the classical limit at $T = 0$ as a consequence of the static molecular disorder of the ice droplet.

V. ENERGETIC PROPERTIES AND DENSITY PROFILES

We turn now to the analysis of the quantum and classical internal energy of ice and water droplets on graphite.

A. Internal energy

The average kinetic and potential energy calculated for the droplet D_{377} on graphite is displayed in Fig. 7 at five temperatures between 50 and 350 K. The results from classical MD simulations are shown by open symbols and those derived from quantum PIMD simulations by closed ones. The ice droplet results correspond to the crystalline structure. In addition, the kinetic energy obtained for ice Ih and water from *NPT* simulations at zero pressure is also plotted.[31,44]

The quantum kinetic energy of the droplets displays a monotonous temperature dependence without apparent discrimination between its solid or liquid behavior between 50 and 350 K (see Fig. 7(a)). The kinetic energy of the droplet has a smooth overlap with that of liquid water. Thus, the kinetic energy does not discriminate between the disorder in either a droplet or bulk liquid water. Ice Ih, with a tetrahedral H-bond network free of defects, has a larger kinetic energy, i.e., about 0.4 kJ/mol above that of the disordered systems at the same temperature. This slight increase in the kinetic energy of ice has been shown to be consistent with the measured isotopic mass dependence of the melting temperature of ice.[44] A recent calculation of the kinetic energy based on optical and inelastic neutron scattering measurements stresses the continuity, within an error margin of about 0.3 kJ/mol in the temperature dependence of the kinetic energy of ice, liquid water, and vapor.[68]

The kinetic energy in the classical limit is displayed in Fig. 7(b). It is identical in the three systems (ice, liquid water,

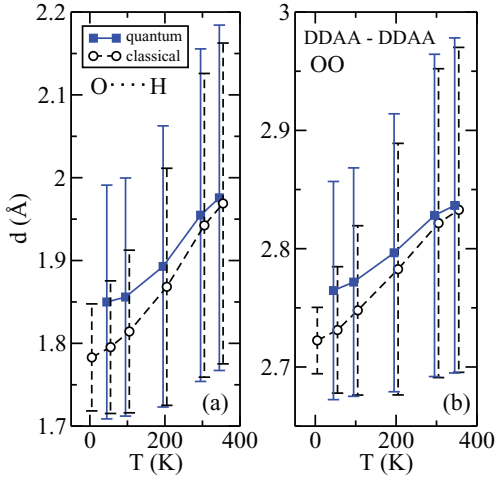

FIG. 6. Average H-bond distances d found in quantum and classical simulations of the droplet D_{377} as a function of temperature. The distance between the H atom and the O acceptor (H···O) is shown in panel (a). The OO distance is shown in panel (b). Both results correspond to DDAA−DDAA bonds. The filled squares in panel (b) are the values given in the DDAA−DDAA row of Table III. The total length of the bars is two times the root mean square fluctuations around the distance d. For the sake of clarity, the quantum (classical) results were mutually displayed by ±5 K.

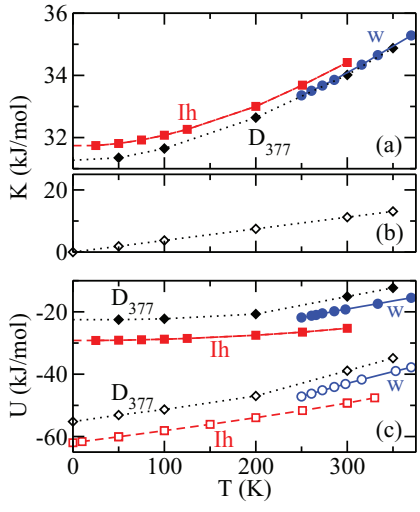

FIG. 7. Kinetic (K) and potential (U) energy of the water droplet D_{337} on graphite as a function of temperature. The droplet results have been compared to those obtained for both ice Ih and liquid water (w) by *NPT* simulations at zero pressure.[31,44] (a) Kinetic energy in the quantum limit; (b) kinetic energy in the classical limit; (c) quantum (closed symbols) and classical (open symbols) potential energy. Note that the energy scale in panel (a) is enlarged by a factor of 10 with respect to the other two. Lines are guides to the eye. The results at 200 K and below correspond to crystalline ice droplets.

and droplet) and obeys the classical equipartition principle of $9k_BT/2$. In the low temperature limit, the quantum kinetic energy of the solid droplet is about 31.2 kJ/mol higher than in the classical limit, while at 300 K this splitting is reduced to about 23 kJ/mol.

Unlike the kinetic energy, the potential energy presented in Fig. 7(c) discriminates between the three systems. The presence of an interface implies a high degree of disorder in the H-bond network of a droplet. At a fixed temperature, this interfacial disorder generates larger potential energies than those found for either ice or water. The temperature dependence of the potential energy of the droplet depends on its solid or liquid character. The slope of $U(T)$ changes from a value similar to the one of ice Ih at temperatures up to 200 K, to an increased slope at temperatures of 300 K and 350 K, similar to the one of bulk water. Relative to the classical potential energy, the quantum results for U are displaced to higher energies. This energy shift is similar to the one found for the kinetic energy.

For the sake of clarity, the results obtained for amorphous ice droplets have not been included in Fig. 7. In the quantum limit, the potential energy U of the amorphous ice droplet is about 1 kJ/mol larger than that of the crystalline ice droplet at the same temperature. The corresponding kinetic energy values differ by about 0.1 kJ/mol, with the lower kinetic energy associated to the amorphous structure. The potential energy between water and the graphite surface has a small contribution to the total potential energy. Below 200 K (i.e., in the crystalline ice droplet) it has a nearly constant value of −1.2 kJ/mol and decreases slightly for the liquid droplet to −1 kJ/mol (300 K) and −0.9 kJ/mol (350 K).

In the classical limit, the sublimation enthalpy of ice Ih at $T = 0$ K, $\triangle H_{sub}(0\,\mathrm{K})$, is equal to the negative of the potential energy. This is true because for the q-TIP4P/F model the zero of the potential energy is set as the energy of an isolated water molecule at $T = 0$ K. The calculated value is 62 kJ/mol (see Fig. 7(c)). In the quantum case, $\triangle H_{sub}(0\,\mathrm{K})$ is the difference between the zero-point energy of an isolated water molecule and that of ice. With the employed potential model the zero-point energy of a water molecule is 50.8 kJ/mol while the value of ice Ih, extrapolated from the kinetic and potential energy data in Figs. 7(a) and 7(c), amounts to 2.6 kJ/mol. Thus, in the quantum limit we obtain $\triangle H_{sub}(0\,\mathrm{K}) = 48.2$ kJ/mol. This value is 13.8 kJ/mol lower than in the classical limit and exhibits reasonable agreement to the tabulation by Feistel and Wagner[69] ($\triangle H_{sub}(0\,\mathrm{K}) = 47.5$ kJ/mol). These authors tabulated the sublimation enthalpy of ice Ih between 0 and 273 K on the basis of experimental and thermodynamic models.[69] Our results show that the empirical water model describes the energetics of H-bonds in condensed phases with better accuracy than for a dimer molecule (see Sec. III A). For the crystalline ice droplet D_{377}, we get in the quantum limit $\triangle H_{sub}(0\,\mathrm{K}) = 42.1$ kJ/mol, a value 13% lower than that of ice Ih. The classical result is significantly larger (55.2 kJ/mol).

B. Density profiles

The probability density perpendicular to the surface of the O and H atoms, $\rho_\perp^O$ and $\rho_\perp^H$, in the D_{377} droplet is presented in Fig. 8 at a temperature of 50 K. The one-dimensional projections are shown along the z-axis, perpendicular to the graphite surface. In Fig. 8(a), the density profile $\rho_\perp^O$ at 50 K indicates that the crystalline ice droplet is made up of five horizontal layers of water molecules parallel to the graphite surface. The vertical separation between layers amounts to about 3.6 Å and the density profile $\rho_\perp^O$ of each layer is split into two peaks. In the initial droplet configuration, these layers correspond to the crystallographic 0001 planes of ice Ih (see Sec. IV A and Fig. 3). The O atoms in these basal planes form non-planar hexagon rings having a chair conformation.[70] A side view of such chair-like hexagons can be seen in the droplet of Fig. 3. In spite of the molecular disorder, one identifies that the O atoms of a layer form a zigzag arrangement exhibiting alternating heights with respect to the graphite surface. This can be identified in the first layer on top of the graphite surface, most clearly in the middle of the layer. The splitting of the density profile, $\rho_\perp^O$, of a layer into two peaks is a fingerprint for the presence of non-planar chair-like rings of O atoms in the crystalline solid droplet. This splitting is clearly seen in Fig. 8(a). The maxima of the first two peaks of the $\rho_\perp^O$ curve are found at heights $z = 3.0$ and 3.7 Å, respectively.

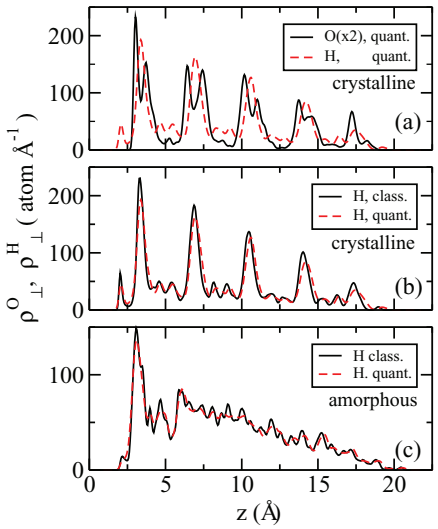

FIG. 8. Profile of the atomic densities perpendicular to the surface. The results correspond to crystalline and amorphous ice droplets, D_{377}, on graphite at 50 K. (a) Quantum profiles for O and H in the crystalline ice droplet. The curve for O has been scaled by a factor of 2; (b) quantum and classical results for H in the crystalline ice droplet; (c) quantum and classical H profiles for the amorphous ice droplet.

Planar hexagonal rings have been observed experimentally by Kimmel et *al.* in ice films grown on graphene over a substrate of Pt(111).[71] This ice polymorph consists of two flat hexagonal sheets of water molecules in which the hexagons in each sheet are stacked directly on top of each other at a distance of about 2.9 Å. This two-layer ice maximizes the number of H-bonds at the expense of adopting a non-tetrahedral geometry with weakened H-bonds.[71] A recent DFT study finds that a planar hexagonal bilayer of ice adsorbed on graphene is more stable than two hexagonal 0001 puckered layers of ice Ih.[14] This result is in agreement with the experimental findings by Kimmel et *al.*[71] However, if the thickness of the ice films increases to four layers, the planar

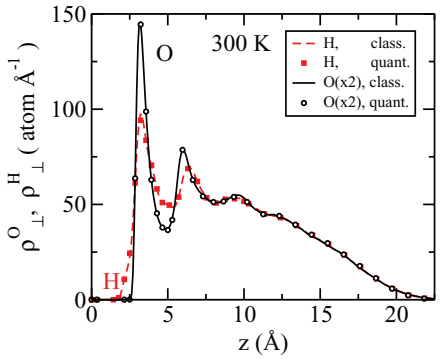

FIG. 9. Profile of the H and O atomic densities perpendicular to the surface. The results correspond to quantum and classical simulations of the droplet D_{377} on graphite at 300 K (liquid droplet). The results for O have been scaled by a factor of 2. The quantum and classical results are identical within the statistical uncertainty of the simulation. Error bars are lower than the displayed symbols.

bilayer structure becomes unstable with respect to four layers of ice Ih.[14] Our calculated probability density profiles support the absence of planar hexagonal rings in the structure of ice droplets in the studied temperature range between 50 and 200 K.

The density profile, $\rho^H_\perp$, of the H atoms is determined by the topology of the H-bond network in the crystalline solid droplet. H-bonds connecting the O atoms of a puckered layer give rise to a peak in the middle of the double-peaks of $\rho^O_\perp$ (see Fig. 8(a)). For the water layer nearest to graphite, the maximum of this H peak appears at 3.4 Å. H-bonds between O atoms in contiguous layers are located at z-coordinates corresponding to the interlayer region, where the $\rho^O_\perp$ curves display low probability density. These H-bonds are responsible for the small peaks in the interlayer region of Fig. 8(a).

The differences between quantum and classical results for $\rho^H_\perp$ and $\rho^O_\perp$ are small at 50 K. The quantum $\rho^H_\perp$ curve in Fig. 8(b) shows that the crystalline ice droplet is slightly expanded in comparison to the classical one. Relative to the z-coordinates of the classical peaks, the quantum $\rho^H_\perp$ are shifted by about 0.1–0.2 A toward larger values. The quantum and classical density profiles of H atoms obtained for the amorphous ice droplet at 50 K are displayed in Fig. 8(c). The effect of molecular disorder is evident by a comparison with the crystalline data in Fig. 8(b). The classical and quantum results reveal differences that are small in the scale of the figure.

The atomic density profiles of crystalline ice droplets at temperatures up to 200 K are qualitatively similar to those presented at 50 K. However, at 300 K the atomic density profiles change drastically as shown in Fig. 9. The $\rho^O_\perp$ and $\rho^H_\perp$ profiles reveal a liquid droplet where molecular disorder has erased the highly structured profile of a crystalline solid drop. A layered ordering is formed in the neighborhood of the graphitic surface. This refers to a packing effect present in all solid-liquid interfaces including droplets.[72] The z-coordinates of the first two maxima are at 3.3 and 6.4 Å, respectively. Interestingly, the density profile curves become identical in the quantum and classical simulations. The quantum-classical differences in the atomic densities of ice droplets vanish in the case of liquid droplets.

The agreement between the quantum and classical $\rho^O_\perp$ and $\rho^H_\perp$ curves of liquid droplets is only found after long simulation runs of at least 12 ns. Such a long time is required to average the significant fluctuations in the shape of the D_{337} droplets. At shorter simulation times of 1–2 ns, one may observe differences between the quantum and classical density profiles due to insufficient sampling. With samplings of 12 ns at 300 K we have found identical quantum and classical density profiles, within the statistical limits, for the droplets D_{187} and D_{377}. For the larger droplets D_{678} and D_{1071}, the quantum simulations of 3 ns were too short to observe the same statistical accuracy in their density profiles as derived in the longer classical runs of 12 ns. We have not tried to perform longer quantum runs for the larger droplets because of their high computational cost. We assume that the result obtained in the long simulation runs of the two smaller droplets is a strong indication of its validity for larger droplet sizes.

VI. DROPLET LIQUID-VAPOR INTERFACE

A. Interface analysis

The density profiles studied in Sec. V B do not provide precise information on the liquid-vapor interface. Therefore, we now want to address the question, if there are significant differences in the classical and quantum liquid-vapor interface of the droplets. To this aim the location of the equimolecular dividing surface is studied by the same procedure as employed in previous classical simulations.[17,72–74] First, the z-axis is set as the surface normal passing through the center-of-mass of the droplet; the distance to this axis is denoted as R. As the equilibrium shape of the droplet displays radial symmetry around the z-axis, the molecular density is analyzed by considering volume elements defined by a cylindrical binning. The reason for using this shape instead of spherical shells is that we do not make the *a priori* assumption of having spherical droplet shapes, as non spherical segment-shaped droplets have been reported for particles interacting through two-body LJ forces.[72] Bins of identical volume are defined with a discretized height of $\triangle z = 0.2$ Å. The radial boundaries are located at $R_i = \sqrt{i \triangle A/\pi}$ for $i = 1, \ldots, N_{max}$ with a base area per bin of $\triangle A = 9\pi$ Å. With this definition, each cylindrical bin of a discretized horizontal layer has a volume of 1.8π Å^3. The molecular density $\rho^O(R)$ for every single layer z of the binned droplet is calculated on the basis of the O coordinates. The location of the equimolecular dividing surface is determined by assuming a tanh function across the liquid-vapor interface[17,72–74]

$$\rho^O(R) = \frac{\rho^O_z}{2}\left[1 - \tanh\left(\frac{2(R - R_z)}{d_z}\right)\right]. \qquad (4)$$

ρ^O_z is the molecular density of the liquid droplet at height z, R_z is the radius defining the equimolecular dividing surface at z, and d_z is a measure of the interface width at z. For a graphical representation of d_z, see Fig. 10. Within the interval $2d_z$ the water density is reduced from the bulk to the gas phase value. In the interphase region, the density of the gas phase is assumed, in agreement with the simulations, to be vanishingly small.

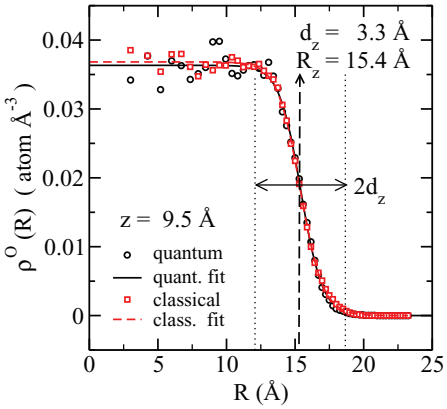

FIG. 10. Radial density of the O atoms as derived at 300 K from quantum (circles) and classical (squares) simulations of the droplet D_{377} on graphite. The volume density was calculated at the horizontal layer $z = 9.5 \pm 0.1$ Å. The simulated densities have been fitted to a tanh function. R_z is the position of the equimolecular dividing surface, where the interface density is half of the bulk liquid density. The width of the liquid-vapor interface is roughly given by $2d_z$. The quantum and classical fits are nearly indistinguishable.

The result for $\rho^O(R)$ at 300 K derived by quantum and classical simulations of the droplet D_{377} on graphite is presented in Fig. 10 at a height $z = 9.5$ Å. The position of the equimolecular dividing surface is obtained by the tanh fit at $R_z = 15.4$ Å, while the parameter d_z is 3.3 Å. Note that the quantum and classical findings are nearly indistinguishable.

The results of the analysis of the liquid-vapor interface as a function of the height z is presented in Fig. 11. The position of the equimolecular dividing surface R_z is displayed in Fig. 11(a). The quantum and classical results are identical within the statistical uncertainty of the simulations. Error bars are low because the long simulation run allows for an efficient sampling of the droplet shape fluctuations and the disorder in the liquid droplet. Larger statistical errors are found at the top

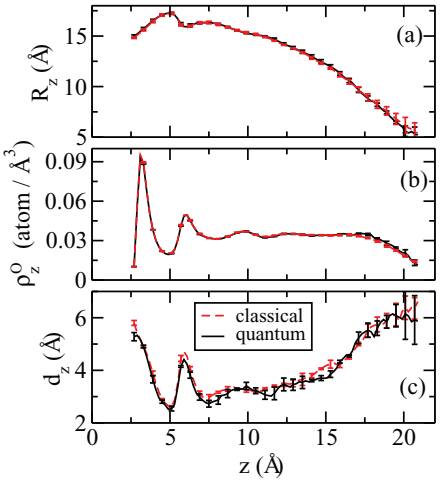

FIG. 11. Results of the 300 K fit of the liquid-vapor interface of the water droplet D_{377} by a tanh function. Both quantum and classical simulation results are given as full and broken lines, respectively. From bottom to top: (a) position of the equimolecular surface, R_z, for horizontal layers at a height z from the graphite surface; (b) volume density of the liquid phase; (c) parameter d_z associated to the interface width. The error bars indicate the statistical uncertainty of the results. In panels (a) and (b), the quantum and classical results are nearly indistinguishable.

of the droplets, i.e., at z-values where the sampled horizontal layer is inside the liquid-vapor interface. Note the different scale of the two axes in Fig. 11(a), so that the droplet shape defined by the R_z profile appears distorted. The graphite surface has a notorious effect in the shape of the droplet at heights $z <$ 7 Å. The fitted liquid density, ρ_z^O, is presented in Fig. 11(b). We find again that the quantum and classical results are identical within the statistical uncertainty of the simulation.

To test the internal consistency of the fitted functions, the quantities R_z and ρ_z^O should be correlated with the atomic density profile $\rho_\perp^O$ shown by a continuous line in Fig. 9. At a given height z, these quantities are related by the expression

$$\rho_\perp^O = \pi R_z^2 \rho_z^O. \tag{5}$$

We have checked that the fitted values of ρ_z^O and R_z satisfy this consistency test.

The width d_z associated to the liquid-vapor interphase is presented in Fig. 11(c). The small differences between the quantum and classical results for d_z are not statistically significant. The parameter d_z shows oscillations at heights below 7 Å that correlate with the density oscillations caused by the hard graphite surface. At higher values of z, the increase in the parameter d_z is a consequence of the interface analysis using horizontal layers. Strictly speaking, the interfacial thickness should be always measured perpendicular to the interface.[73]

The interfacial water structures of H_2O and D_2O are indistinguishable as derived in recent quantum PIMD simulations of a planar interfaces.[25] This absence of an isotope effect is in line with the indistinguishability of the liquid-vapor interface in our quantum and classical simulations of droplet interfaces. Nevertheless, the simulations of Ref. 25 predict an isotope effect in the case of HDO molecules. The intramolecular symmetry breaking is reflected in the interface, so that the OH bonds are preferably oriented into the vapor phase. These simulation results show good agreement to vibrational sum-frequency generation spectroscopy.[25] The relative preference for D to occupy H-bonded rather than dangling positions was also predicted by Anick in the study of the zero-point energy of water clusters by a harmonic approximation in combination with DFT calculations.[63]

The comparison of the liquid-vapor interface in the quantum and classical simulations of the droplet D_{187} at 300 K leads to results in agreement to those presented for the larger droplet, D_{377}. This can be considered as a justification that the indistinguishability of the liquid-vapor interface in the quantum and classical simulations of water droplets at 300 K is a size independent result. For this reason, the analysis of the contact angle and the line tension as a function of the droplet size is presented in Subsections VI B and VI C on the basis of only classical simulations.

B. Contact angle

We employ the same procedure as in Refs. 17, 73, and 74 for the calculation of the contact angle between the droplet and the graphite surface. The droplet shape R_z obtained from the tanh function in Eq. (4) is fitted to a circle with radius R_d

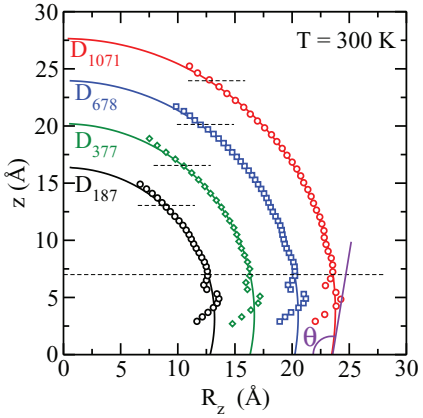

FIG. 12. Correlation between the droplet shapes R_z and the separation z from the surface. The open symbols refer to R_z as derived from the classical simulations of the four studied droplet sizes at 300 K. Full lines are circular shapes fitted to R_z. The fits were limited to a region 7 Å $< z < z_{max}$. The limits are shown by broken lines. The short ones indicate the z_{max} used for each droplet. The contact angle θ is defined by the tangent of the circle at $z = 0$.

that is centered at a height z_d

$$(z - z_d)^2 + R_z^2 = R_d^2 \, . \tag{6}$$

The full lines in Fig. 12 display the fitted spherical shapes of the droplets as derived from the classical simulations at 300 K. Open symbols are R_z values derived from Eq. (4). Heights in the range 7 Å $< z < z_{max}$ were used in the fit. The lowest cut-off avoids the oscillations in R_z caused by the graphite surface. The upper limit z_{max} excludes the top of the droplet, where the statistical error of R_z is largest (see Fig. 11(a)). From our simulations, we conclude that the equilibrium droplet shape is a spherical cap. The same result has been observed quite frequently in other classical simulations of water droplets on surfaces.[74,75] However, a simulation of LJ particles on a solid surface has shown droplets which are not spherically shaped.[72]

The fitted z_d and R_d values as well as some relevant geometrical data of the spherical caps are summarized in Table IV. The contact angle θ, calculated at $z = 0$ (see Fig. 12), decreases as the size of the drop increases, in agreement to the simulations reported in Ref. 75. The contact circle of the spherical cap with graphite has radius, R_b, and its surface is S_b. The external surface of the spherical cap, excluding the base S_b, is S_{cap}. We observe that the ratio S_{cap}/S_b converges with the size of the droplet to a value of 2.4. The ratio between the volume of the spherical cap and the volume of the whole sphere tends to a value slightly larger that 0.6.

C. Line tension

The modified Young's equation for a spherical droplet with contact angle θ and a circular contact line of radius R_b is given as[17,76]

$$\cos\theta = \cos\theta_\infty - \frac{\tau}{\gamma}\frac{1}{R_b} \, , \tag{7}$$

where θ_∞ is the contact angle of an infinitely large droplet, τ is the line tension, and γ the liquid-vapor surface tension.

TABLE IV. Results of the fit of a spherical shape for the liquid droplets studied by classical simulations at 300 K. z_d and R_d are the height of the center of the sphere and its radius, respectively. θ is the value of the contact angle. Estimated statistical errors are ±0.3 Å for the distances (z_d, R_d) and ±2° for the contact angle. The equilibrium droplet shape is a spherical cap. Several geometrical parameters of the droplet are given: R_b and S_b are the radius and area of the contact circle at $z = 0$. S_{cap} (without including S_b) and V_{cap} denote the surface and volume of the spherical cap. V_{sph} is the volume of the sphere.

	D_{187}	D_{377}	D_{678}	D_{1071}
z_d (Å)	3.2	3.5	3.4	3.9
R_d (Å)	13.2	16.7	20.5	23.8
θ (deg)	104	102	100	99
R_b (Å)	12.8	16.3	20.2	23.5
S_b (Å^2)	516	836	1287	1730
S_{cap} (Å^2)	1359	2116	3091	4130
S_{cap}/S_b	2.6	2.5	2.4	2.4
V_{cap}/V_{sph}	0.68	0.65	0.62	0.62

The results for $\cos\theta$ and R_b from Table IV are represented in Fig. 13. The extrapolated value of the contact angle θ_∞ amounts to 93° ± 3°. This value is larger than the reported contact angle for the SPC/E model,[77,78] which should be attributed to differences in the employed water force field. The slope is negative which implies that the line tension τ is positive. By considering the experimental surface tension of water at 300 K, $\gamma = 72$ mN/m, we derive a line tension of 1.7 $\times 10^{-11}$ J/m. It should be noted that the sign and magnitude of the line tension are in agreement with the recent work of Dutta and co-workers[77,78] and with Ref. 75. However, our current value is somewhat lower than the line tension of the SPC/E model (∼2.4–3.0 $\times 10^{-11}$ J/m).[17,77,78] In view of the differences in the model parameters (rigid SPC/E vs. flexible q-TIP4P/F water potential, 80% lower ϵ_{CO} parameter, and different droplet sizes), we conclude that the agreement is reasonable. In fact, not only the magnitude but even the sign of the line tension has been subject of debate.[72,79] Recent MD simulations of water droplets on graphene using a SCP model report a negative line tension of -3×10^{-11} J/m.[23] Studies of

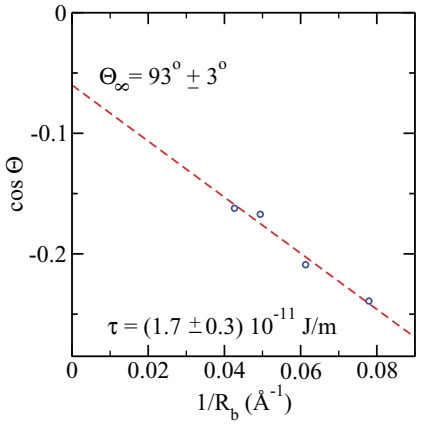

FIG. 13. Cosine of the contact angle, θ, of water droplets on graphite as a function of the inverse base radius R_b which has been derived from our classical simulations at 300 K. The broken line is the linear fit with Eq. (7). The fitted parameters are the macroscopic contact angle θ_∞ and the line tension τ.

LJ particles on a solid surface predict a negative line tension for the drops as well.[72,80]

VII. CONCLUSIONS

Quantum PIMD and classical MD simulations of water droplets on graphite have been performed to assess the importance of nuclear quantum effects in the droplet as a function of temperature. We have used the flexible q-TIP4P/F water model and a LJ potential to describe water-carbon interactions. In the low-temperature limit, a quantum description of the atomic nuclei leads to a surface binding energy of the water molecule that is three times smaller than the binding energy of two water molecules in a water dimer. Quantum zero-point motions reduce the classical binding energy of a water dimer by 32%, and the surface binding energy by 7%. With increasing temperature, however, these differences become smaller, in particular for the weak water-graphite interaction. At 50 K the surface binding energy in the quantum case is only 1% lower than in the classical limit.

We have studied water droplets at temperatures where the droplet is either solid or liquid. The initial geometry for the solid droplets was generated from the ice Ih structure by considering clusters formed under inclusion of the successive coordination spheres of a central water molecule. The spherical clusters were cut by a plane perpendicular to the hexagonal axis of ice Ih to get spherical caps made up of layers of water molecules with 0001 orientation. After a geometry optimization of the ice droplets on graphite, the calculation of their vibrational density of states allowed us to identify the main differences with ice Ih. Particularly interesting is the effect of the presence of dangling OH bonds and the deviation from a tetrahedral H-bond framework in the vibrational properties. Initial geometries of amorphous ice droplets were generated by sudden cooling of liquid droplets. The molecular disorder in the amorphous droplet causes a red shift of the vibrational states associated to the intermolecular librational modes and a concomitant blue shift of the intramolecular OH stretching vibrations. This effect is in line with a weakening of the H-bonds in the amorphous ice structure relative to the crystalline one.

In quantum simulations, the average distance of covalent OH bonds displays temperature independent mean square fluctuations of 0.07 Å, which is a consequence of the zero-point vibrations. OH dangling bonds are shorter than non-dangling ones. These covalent bonds differ in their temperature dependence. Average dangling bond distances are temperature independent, while non-dangling bonds become shorter with increasing temperature. This effect is a consequence of the coupling between OH and H-bonds. Classically, average OH distances are 0.01 Å shorter than in the quantum case. At 50 K the classical average of the bridging OO distances is 0.03 A shorter than the quantum value. But as expected this difference decreases with increasing temperature.

The temperature dependence of the kinetic and potential energy of the water droplets on graphene was compared to that of ice Ih and liquid water, in both the quantum and classical limits. At a given temperature, the kinetic energy of ice Ih in the quantum simulations is slightly higher than that one of the disordered systems (droplet, liquid). The kinetic energy is not sensitive to the different kinds of disorder in a droplet (presence of an interface) and in the bulk liquid (without interface). On the contrary, the calculated potential energy is found to increase in the order ice Ih < bulk liquid < droplet.

The analysis of atomic density profiles of the droplets shows differences between the quantum and classical simulations at temperatures where the droplet is solid. In the quantum limit, they are slightly expanded relative to the classical result. However, the results at 300 and 350 K, where the droplet is liquid, show that the density profiles and the liquid-vapor interface of the droplet are identical within the statistical uncertainty of the simulations in the quantum and classical limits. The equilibrium shape of the studied droplets is a spherical cap. This result has been found in droplets with a number of water molecules in the range 100–1000. The contact angle of the droplet decreases with the droplet size. The simulation data can be extrapolated to a macroscopic value of $\theta_\infty = 93^\circ \pm 3^\circ$. The calculated line tension is positive and amounts to $(1.7 \pm 0.3) \times 10^{-11}$ J/m. From the present approach, we also deduce that the adopted classical simulation technique is of sufficient accuracy for the study of certain interfacial properties despite the light water hydrogens. It seems that the sizeable importance of zero-point fluctuations does not affect collective, i.e., macroscopic, properties such as the contact angle.

ACKNOWLEDGMENTS

This work was supported by MEC (Spain) through Grant No. FIS2012-31713 and by the DFG priority program 1369 "Polymer-solid contacts: Interfaces and interphases." J.K.S. thanks the Alexander von Humboldt Foundation for financial support. We thank Dr. Frédéric Leroy for a critically reading of the paper and useful suggestions.

[1] C. Tanford, Science **200**, 1012 (1978).
[2] M. A. Henderson, Surf. Sci. Rep. **46**, 1 (2002).
[3] D. Chandler, Nature (London) **437**, 640 (2005).
[4] N. Giovambattista, P. J. Rossky, and P. G. Debenedetti, Phys. Rev. Lett. **102**, 050603 (2009).
[5] G. Cicero, J. C. Grossman, E. Schwegler, F. Gygi, and G. Galli, J. Am. Chem. Soc. **130**, 1871 (2008).
[6] A. A. Balandin, Nat. Mater. **10**, 569 (2011).
[7] A. H. Castro Neto, F. Guinea, N. M. R. Peres, K. S. Novoselov, and A. K. Geim, Rev. Mod. Phys. **81**, 109 (2009).
[8] I. W. Frank, D. M. Tanenbaum, A. M. van der Zande, and P. L. McEuen, J. Vac. Sci. Technol. B **25**, 2558 (2007).
[9] V. Singh, D. Joung, L. Zhai, S. Das, S. I. Khondaker, and S. Seal, Prog. Mater. Sci. **56**, 1178 (2011).
[10] X. Liu, M. Wang, S. Zhang, and B. Pan, J. Environ. Sci. **25**, 1263 (2013).
[11] C. Soldano, A. Mahmood, and E. P. Dujardin, Carbon **48**, 2127 (2010).
[12] D. Berman, A. Erdemir, and A. V. Sumant, Mater. Today **17**, 31 (2014).
[13] E. Celia, T. Darmanin, E. T. de Givenchy, S. Amigoni, and F. Guittard, J. Colloid Interface Sci. **402**, 1 (2013).
[14] D. J. Anick, J. Phys. Chem. A **118**, 7498 (2014).
[15] A. Ambrosetti, F. Ancilotto, and P. L. Silvestrelli, J. Phys. Chem. C **117**, 321 (2013).
[16] J. K. Singh and F. Müller-Plathe, Appl. Phys. Lett. **104**, 021603 (2014).
[17] T. Werder, J. H. Walther, R. L. Jaffe, T. Halicioglu, and P. Koumoutsakos, J. Phys. Chem. B **107**, 1345 (2003).
[18] M. C. Gordillo and J. Martí, J. Phys.: Condens. Matter **22**, 284111 (2010).

[19]H. Zhou, P. Ganesh, V. Presser, M. C. F. Wander, P. Fenter, P. R. C. Kent, D. Jiang, A. A. Chialvo, J. McDonough, K. L. Shuford *et al.*, Phys. Rev. B **85**, 035406 (2012).
[20]J. Rafiee, X. Mi, H. Gullapalli, A. V. Thomas, F. Yavari, Y. Shi, P. M. Ajayan, and N. A. Koratkar, Nat. Mater. **11**, 217 (2012).
[21]H. Li and X. C. Zeng, ACS Nano **6**, 2401 (2012).
[22]M. K. Rana and A. Chandra, J. Chem. Phys. **138**, 204702 (2013).
[23]C.-J. Shih, Q. H. Wang, S. Lin, K.-C. Park, Z. Jin, M. S. Strano, and D. Blankschtein, Phys. Rev. Lett. **109**, 176101 (2012).
[24]F. Taherian, V. Marcon, N. F. A. van der Vegt, and F. Leroy, Langmuir **29**, 1457 (2013).
[25]Y. Nagata, R. E. Pool, E. H. G. Backus, and M. Bonn, Phys. Rev. Lett. **109**, 226101 (2012).
[26]R. Ramírez, J. Schulte, and M. C. Böhm, Mol. Phys. **99**, 1249 (2001).
[27]M. C. Böhm, R. Ramírez, and J. Schulte, Mol. Phys. **103**, 2407 (2005).
[28]M. C. Böhm, R. Ramírez, and J. Schulte, Chem. Phys. **342**, 1 (2007).
[29]B. Pamuk, J. M. Soler, R. Ramírez, C. P. Herrero, P. W. Stephens, P. B. Allen, and M.-V. Fernández-Serra, Phys. Rev. Lett. **108**, 193003 (2012).
[30]R. Ramírez and C. P. Herrero, J. Chem. Phys. **133**, 144511 (2010).
[31]C. P. Herrero and R. Ramírez, J. Chem. Phys. **134**, 094510 (2011).
[32]S. Habershon, T. E. Markland, and D. E. Manolopoulos, J. Chem. Phys. **131**, 024501 (2009).
[33]R. Raj, S. C. Maroo, and E. N. Wang, Nano Lett. **13**, 1509 (2013).
[34]Z. Li, Y. Wang, A. Kozbial, F. Zhou, R. McGinley, P. Ireland, B. Morganstein, A. Kunkel, S. P. Surwade, L. Li *et al.*, Nat. Mater. **12**, 925 (2013).
[35]R. P. Feynman, *Statistical Mechanics* (Addison-Wesley, New York, 1972).
[36]M. J. Gillan, Philos. Mag. A **58**, 257 (1988).
[37]D. M. Ceperley, Rev. Mod. Phys. **67**, 279 (1995).
[38]C. Chakravarty, Int. Rev. Phys. Chem. **16**, 421 (1997).
[39]C. Herrero and R. Ramírez, J. Phys.: Condens. Matter **26**, 233201 (2014).
[40]M. E. Tuckerman, B. J. Berne, G. J. Martyna, and M. L. Klein, J. Chem. Phys. **99**, 2796 (1993).
[41]M. E. Tuckerman and A. Hughes, in *Classical and Quantum Dynamics in Condensed Phase Simulations*, edited by B. J. Berne and D. F. Coker (World Scientific, Singapore, 1998), p. 311.
[42]G. J. Martyna, A. Hughes, and M. E. Tuckerman, J. Chem. Phys. **110**, 3275 (1999).
[43]M. E. Tuckerman, in *Quantum Simulations of Complex Many-body Systems: From Theory to Algorithms*, edited by J. Grotendorst, D. Marx, and A. Muramatsu (NIC, FZ Jülich, 2002), p. 269.
[44]R. Ramírez and C. P. Herrero, Phys. Rev. B **84**, 064130 (2011).
[45]C. P. Herrero and R. Ramírez, Phys. Rev. B **84**, 224112 (2011).
[46]R. Ramírez, N. Neuerburg, and C. P. Herrero, J. Chem. Phys. **137**, 134503 (2012).
[47]M. F. Herman, E. J. Bruskin, and B. J. Berne, J. Chem. Phys. **76**, 5150 (1982).
[48]M. Parrinello and A. Rahman, J. Chem. Phys. **80**, 860 (1984).
[49]W. Klopper, J. G. C. M. van Duijneveldt-van de Rijdt, and F. B. van Duijneveldt, Phys. Chem. Chem. Phys. **2**, 2227 (2000).
[50]A. Shank, Y. Wang, A. Kaledin, B. J. Braams, and J. M. Bowman, J. Chem. Phys. **130**, 144314 (2009).
[51]B. E. Rocher-Casterline, L. C. Ch'ng, A. K. Mollner, and H. Reisler, J. Chem. Phys. **134**, 211101 (2011).
[52]O. Leenaerts, B. Partoens, and F. M. Peeters, Phys. Rev. B **79**, 235440 (2009).
[53]J. Ma, A. Michaelides, D. Alfè, L. Schimka, G. Kresse, and E. Wang, Phys. Rev. B **84**, 033402 (2011).
[54]D. Feller and K. D. Jordan, J. Phys. Chem. A **104**, 9971 (2000).
[55]V. M. Bermudez and J. T. Robinson, Langmuir **27**, 11026 (2011).
[56]M. Rubeš, P. Nachtigall, J. Vondrášek, and O. Bludský, J. Phys. Chem. C **113**, 8412 (2009).
[57]E. Voloshina, D. Usvyat, M. Schutz, Y. Dedkov, and B. Paulus, Phys. Chem. Chem. Phys. **13**, 12041 (2011).
[58]V. Buch, P. Sandler, and J. Sadlej, J. Phys. Chem. B **102**, 8641 (1998).
[59]G. P. Johari, J. Chem. Phys. **109**, 1070 (1998).
[60]S. Kirkpatrick, C. D. Gelatt, and M. P. Vecchi, Science **220**, 671 (1983).
[61]See supplementary material at http://dx.doi.org/10.1063/1.4901562 for a set of ascii files with the optimized structures of the studied droplets. For each file, the first line contains the number of atoms. The following lines contain the atomic symbol and cartesian coordinates (in Å) of all atoms.
[62]A. Luzar and D. Chandler, J. Chem. Phys. **98**, 8160 (1993).
[63]D. J. Anick, J. Chem. Phys. **123**, 244309 (2005).
[64]Y. R. Shen and V. Ostroverkhov, Chem. Rev. **106**, 1140 (2006).
[65]A. Politano, A. R. Marino, V. Formoso, and G. Chiarello, Carbon **49**, 5180 (2011).
[66]J. A. Morrone and R. Car, Phys. Rev. Lett. **101**, 017801 (2008).
[67]U. Bergmann, A. Di Cicco, P. Wernet, E. Principi, P. Glatzel, and A. Nilsson, J. Chem. Phys. **127**, 174504 (2007).
[68]Y. Finkelstein and R. Moreh, Chem. Phys. **431–432**, 58 (2014).
[69]R. Feistel and W. Wagner, Geochim. Cosmochim. Acta **71**, 36 (2007).
[70]A. von Hippel and E. F. Farrell, Mater. Res. Bull. **8**, 127 (1973).
[71]G. A. Kimmel, J. Matthiesen, M. Baer, C. J. Mundy, N. G. Petrik, R. S. Smith, Z. Dohnálek, and B. D. Kay, J. Am. Chem. Soc. **131**, 12838 (2009).
[72]T. Ingebrigtsen and S. Toxvaerd, J. Phys. Chem. C **111**, 8518 (2007).
[73]M. J. de Ruijter, T. D. Blake, and J. De Coninck, Langmuir **15**, 7836 (1999).
[74]S. Khan and J. K. Singh, Mol. Simul. **40**, 458 (2014).
[75]T. Werder, J. H. Walther, R. L. Jaffe, T. Halicioglu, and P. Koumoutsakos, J. Phys. Chem. B **112**, 14090 (2008).
[76]J. Y. Wang, S. Betelu, and B. M. Law, Phys. Rev. E **63**, 031601 (2001).
[77]R. C. Dutta, S. Khan, and J. K. Singh, Fluid Phase Equilib. **302**, 310 (2011).
[78]R. C. Dutta, S. Khan, and J. K. Singh, Fluid Phase Equilib. **334**, 205 (2012).
[79]Q. Wang and J. K. Johnson, Fluid Phase Equilib. **132**, 93 (1997).
[80]J. Zhang, F. Leroy, and F. Müller-Plathe, Phys. Rev. Lett. **113**, 046101 (2014).